Water UV-shielding in the Terrestrial Planet-forming Zone: Implications for Carbon Dioxide Emission

Arthur D. Bosman , Edwin A. Bergin , Jenny K. Calahan , and Sara E. Duval
University of Michigan, LSA Astronomy, 1085 S University, Ann Arbor, MI 48109, USA; arbos@umich.edu

Abstract

Carbon dioxide is an important tracer of the chemistry and physics in the terrestrial planet-forming zone. Using a thermochemical model that has been tested against the mid-infrared water emission, we reinterpret the CO_2 emission as observed with Spitzer. We find that both water UV-shielding and extra chemical heating significantly reduce the total CO_2 column in the emitting layer. Water UV-shielding is the more efficient effect, reducing the CO_2 column by ∼2 orders of magnitude. These lower CO_2 abundances lead to CO_2-to-H_2O flux ratios that are closer to the observed values, but CO_2 emission is still too bright, especially in relative terms. Invoking the depletion of elemental oxygen outside of the water midplane ice line more strongly impacts the CO_2 emission than it does the H_2O emission, bringing the CO_2-to-H_2O emission in line with the observed values. We conclude that the CO_2 emission observed with Spitzer-IRS is coming from a thin layer in the photosphere of the disk, similar to the strong water lines. Below this layer, we expect CO_2 not to be present except when replenished by a physical process. This would be visible in the $^{13}CO_2$ spectrum as well as certain $^{12}CO_2$ features that can be observed by JWST-MIRI.

Unified Astronomy Thesaurus concepts: Protoplanetary disks (1300); Astrochemistry (75)

1. Introduction

Carbon dioxide, CO_2, is an important molecule in the interstellar inventory. CO_2 is a carrier of significant volatile carbon and oxygen in both interstellar (Boogert et al. 2015) and cometary (Mumma & Charnley 2011) ices. However, the lack of a permanent dipole and its abundance in Earth's atmosphere requires infrared space missions for astronomical observations. The chemistry of CO_2 is closely linked to CO, a common precursor to CO_2 and H_2O, with which CO_2 shares the OH radical as a precursor in both gas and grain-surface chemistry (e.g., Smith et al. 2004; Arasa et al. 2013). Such close chemical links to the main reservoirs of carbon and oxygen make CO_2 an important tracer of the carbon and oxygen elemental abundances, especially the overall C/O ratio. As the C/O ratio is proposed to link planet composition and formation history (Öberg et al. 2011), CO_2 likely has an important role to play in the unraveling of this complex problem.

Toward protoplanetary disks, CO_2 has most commonly been observed in emission using Spitzer-IRS (e.g., Carr & Najita 2008; Pontoppidan et al. 2010). CO_2 emission has been inferred to originate from the warm (>300 K) surface layers confined to within the inner few astronomical units (Salyk et al. 2011; Bosman et al. 2017). In these strongly irradiated disk surface layers, the abundance of CO_2 is sensitive to both the C/O ratio, through the abundance of its precursor OH (e.g., Woitke et al. 2018; Anderson et al. 2021), and the elemental abundance of C (See Figure 1 in Bosman et al. 2018a).

The interplay between dust growth, dynamics, and chemistry in the outer (tens of astronomical units) disk might also significantly impact the abundance of CO_2 in the inner few astronomical units where excitation conditions allow for

detectable rovibrational emission. The low CO abundances in the outer disk are possibly pointing to a sequestration of carbon into CO_2 ices (Eistrup et al. 2016; Bosman et al. 2018b). This is seen in detailed models that link chemistry to dust evolution (Krijt et al. 2020). As these ices drift to inside the CO_2 sublimation front (or ice line), they could greatly impact the inner disk CO_2 abundance (e.g., Bosman et al. 2017; Booth et al. 2017). Thus, CO_2 might be a sensitive tracer of dust drift.

Gas dynamics in the inner few astronomical units could also impact the CO_2 abundance structure. Vertical mixing of water, followed by sequestration on large grains dubbed the "vertical cold finger effect," has been invoked to explain the limited extent of the water surface reservoir (Meijerink et al. 2009; Blevins et al. 2016; Bosman & Bergin 2021), and dynamical simulations have shown it to be effective (Krijt et al. 2016). Such sequestration would similarly affect CO_2 outside of the CO_2 ice line. Furthermore between the H_2O and CO_2 ice lines, the sequestration of water can impact the elemental abundances of carbon and oxygen, creating an environment in which CO_2 is inefficiently formed and the excess oxygen lost to water ice in the midplane.

The abundance of CO_2 is a crucial component in understanding the overall C/O ratio of gas and ices, but it also can be a probe of the overall disk chemical evolution, which is linked to the disk gas and dust physics. To fully understand these processes requires the emission to be analyzed in detail. Unfortunately, recent modeling efforts have difficulty in simultaneously predicting the H_2O and CO_2 fluxes in the mid-infrared (Woitke et al. 2018; Anderson et al. 2021). In this paper, we used an updated set of thermochemical models that has been tested against the infrared water observations (Bosman et al. 2022) to study the CO_2 abundance structure and emission from the inner disk regions. Crucially, our model includes the effects of water UV-shielding. This must be present given the large water columns (Bethell & Bergin 2009) leading to UV absorption at higher surface layers than would

Table 1
Elemental Abundances w.r.t. H

Element	Abundance w.r.t. H
H	1.0
He	7.59×10^{-2}
C	1.35×10^{-4}
N	2.14×10^{-5}
O	2.88×10^{-4}
Mg	4.17×10^{-9}
Si	7.94×10^{-8}
S	1.91×10^{-8}
Fe	4.27×10^{-9}

be set by the dust optical surface to UV photons; this can strongly alter the chemical structure of which CO_2 is a key component.

2. Methods

We use the DALI models from Bosman et al. (2022). These models include modification from standard DALI (Bruderer et al. 2012; Bruderer 2013) to better represent the inner disk regions. This includes more efficient H_2 formation at high temperature, more efficient heating following photodissociation (following Glassgold & Najita 2015), and water UV-shielding (Bethell & Bergin 2009). The models assume the AS 209 spectrum from Zhang et al. (2021) as input. Most of the UV in this spectrum is in Lyα (Herczeg et al. 2004). Four different physical structures are computed, two large grain fractions (99% and 99.9%) and two disk scale heights ($h/R = 0.08$ and 0.16 at $R = 45$ au). Model setup details are in Bosman et al. (2022). The elemental abundances used in the chemistry are given in Table 1. Abundances are based on Jonkheid et al. (2006), with reduced Mg, Si, S, and Fe. As the chemical timescale in the region of interest is short, we solve for statistical equilibrium (Anderson et al. 2021).

From the temperature and CO_2 abundance structure, we calculate the CO_2 emission spectrum using the molecular data as collected and computed in Bosman et al. (2017). The molecular excitation is calculated explicitly by balancing excitation and de-excitation from collisions and photon absorption and emission. Energy levels, line positions, and line strengths are from the HITRAN database (Rothman et al. 2013). Throughout this paper, we use the CO_2 level notation as used in Bosman et al. (2017). When talking about the main CO_2 feature around 15 μm, we denote this as the $01^10 - 00^00$ Q branch, but it is implied that this includes a smaller contribution of the more highly excited $02^20–01^10$, $03^30–02^20$, etc., Q branches.

For comparison with slab excitation models we use the model from Banzatti et al. (2012), using representative slab-model parameters from Salyk et al. (2011). For water, we use a column of 3×10^{18} cm^{-2} and an excitation temperature of 500 K, as done in (Bosman et al. 2022), while for CO_2 we use a column of 3×10^{15} cm^{-2} and a excitation temperature of 700 K. These effectively match the typical H_2O and CO_2 spectra and are excellent proxies for the observed emission spectrum.

3. Results

3.1. CO_2 Abundance

Figure 1 shows the CO_2 abundance structure for the flat model with a large grain fraction of 99.9%. In this baseline model, the CO_2 abundance is roughly distributed in two reservoirs. On the disk surface, there is the warm (>500 K), CO_2 layer with an abundance between 10^{-8}–10^{-6} spanning the entire 0.1–1 au region, with a low-abundance tail to larger radii. Below this is a high-abundance, $>10^{-6}$, cooler (100–500 K) CO_2 region that reaches all the way to the midplane and out to the CO_2 ice line. There is some additional structure as CO_2 vapor is absent in the inner ~0.2 au and in a region around 0.7 au near the disk midplane, the former is caused by carbon sequestration in hydrocarbons, while the latter is caused by the efficient formation of water ice. The high-abundance, cool CO_2 reservoir extends to high in the disk photosphere ($z/r > 0.1$) and contributes to line formation. This CO_2 morphology is identical for the other physical structures.

When H_2O UV-shielding is included, both reservoirs are significantly impacted (see the second panel of Figure 1). The warm surface layer becomes thinner, and the region of high CO_2 abundance ($\sim 10^{-6}$) is restricted to below $z/r \leqslant 0.1$. In this model, CO_2 vapor returns to the high-abundance value around the $\tau_{15\mu m} = 1$ layer. The decrease of the CO_2 abundance is driven by the slower photodissociation of H_2O, leading to lower OH production rates, which is critical for the production of CO_2. Furthermore, the CO_2 dissociation rate is not decreased by the same amounts as the H_2O dissociation rate. Unfortunately, the OH emission from disks is dominated by OH that is above the point where H_2O can start to block the UV radiation, as such OH cannot be used as a tracer of H_2O UV-shielding (see Appendix A).

Increasing the chemical heating after photodissociation only impacts the abundance in the warm surface layer. The increased temperatures increase the efficiency of the $OH + H_2 \rightarrow H_2O + H$ reaction, which has a high reaction barrier (1740 K; Baulch et al. 1992), leaving less OH for the $OH + CO \rightarrow CO_2 + H$ reaction, changing the H_2O to CO_2 abundance ratio (see, e.g., Figure 1 of Bosman et al. 2018a).

Figure 1 also shows the emitting area of the $01^10–00^00$ $R(20)$ line as an irregular red box. This line has an upper-level energy of ~1250 K, of which ~250 K is in rotational energy. This is relatively low in comparison to the nearby water lines, many of which have upper-level energies of >2500 K. The emitting region of this line clearly traces the warm surface layer of the disk and extends over the full radial extent in gas where the CO_2 vapor abundance lies between 10^{-9} to a few $\times 10^{-7}$. Lines with lower rotational excitation will emit from a slightly larger radial region. As can be seen in Figure 1 the CO_2 emitting area extends to layers exterior to the water midplane ice line and, in almost all cases, the CO_2-emitting area is larger than that for the water vapor lines.

Figure 2 shows the gas temperature as a function of the vertical, top-down CO_2 column at the radius of the water ice line. Here, for ease in comparison, we show only two models, both with large grain fractions of 99.9%; one is the base DALI model and the other with extra chemical heating and water UV-shielding. These two models show sharply different structures. In the nonshielding model, CO_2 is abundant throughout the full vertical extent of the disk, so the temperature decreases relatively smoothly with increasing CO_2 column. In the water
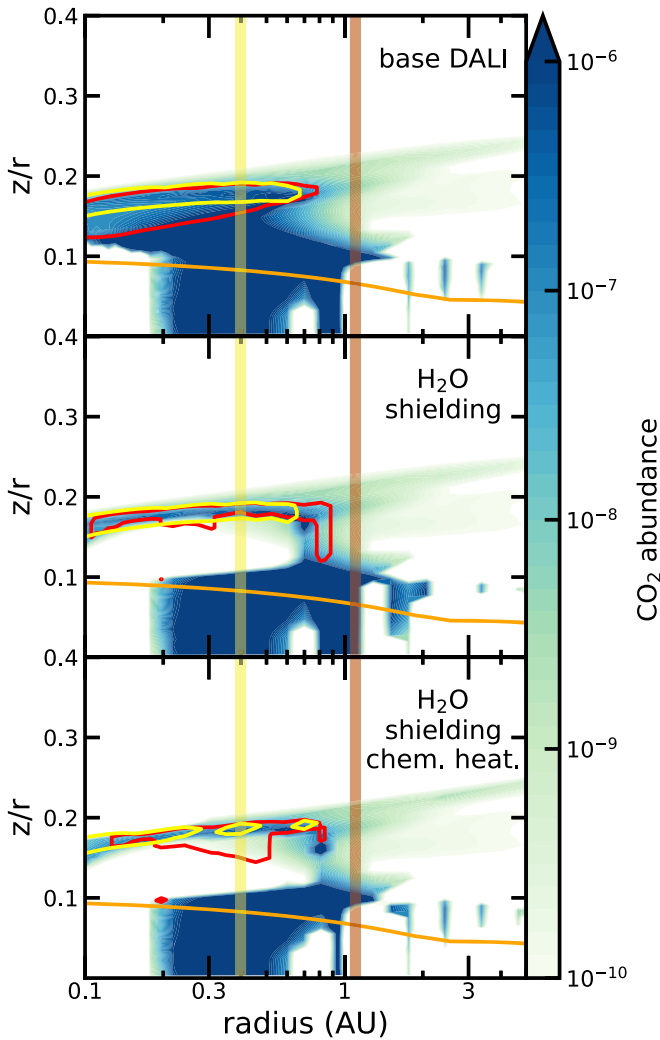
Figure 1. CO_2 abundance for the thin model with a large grain fraction of 99.9% for variation in the thermochemical model. The red contour shows the region from which 90% of the CO_2 $01^10–00^00$ $R(20)$ emission line originates, the yellow contour shows the region from which 90% of the H_2O $11_{3,9}–10_{0,10}$ line flux at 17.2 μm originates, the orange line shows the continuum $\tau_{15\mu m} = 1$ surface, and the vertical yellow and red bands show the locations of the H_2O (0.4 au) and CO_2 (1.2 au) midplane ice lines, respectively.

UV-shielding model, CO_2 is absent in the intermediate layers. As a result, the temperature drops sharply when the column reaches around 10^{16} cm^{-2}. The low CO_2 abundance in the intermediate layers is caused by the UV-shielding of water. The self-shielding of water stops the formation of OH, inhibiting the formation of CO_2. As CO_2 can dissociate at longer wavelengths compared to H_2O, dissociation of CO_2 is still possible; together, this strongly lowers the CO_2 abundance. In the deeper layers, all UV is blocked by the small dust. In these layers, which have very high density, the statistical equilibrium that is calculated tends toward the chemical equilibrium.

This abundance and temperature structure strongly constrains where the emission in the water UV-shielded model can originate from. Only a column of ~10^{16} cm^{-2} can contribute to the emission. CO_2 deeper into the disk exists at much lower temperatures, as well as at temperatures close to the $\tau_{15\mu m} = 1$ surface (~200 K). Contribution for columns >10^{16} cm^{-2} should thus be negligible. Contrast this with the models without shielding, where the temperature is ~300 K at a

column of 10^{18}, so two orders of magnitude higher columns can contribute to the emission in this model.

3.2. CO₂ Spectra

Figure 3 shows the H_2O and CO_2 spectra around the 15 μm CO_2 vibrational band. The baseline DALI models predict relatively stronger CO_2 emission when compared to the surrounding H_2O line forest. The CO_2 $01^10–00^00$ Q branch is a factor of few brighter than the surrounding water lines, and the individual CO_2 $01^10–00^00$ P and R branch lines are on par with the water lines. Both of these characteristics are inconsistent with Spitzer/IRS observations of typical disk systems as exemplified by the slab models in Figure 3.

Including water UV-shielding reduces the CO_2 flux. This is a direct consequence of the thinner upper atmosphere CO_2 layer. As the water emission is less strongly affected by the inclusion of water UV-shielding (Bosman et al. 2022), the ratio between water and CO_2 lines gets closer to the ratio in the slab models, but (in a relative sense) CO_2 emission is still too bright.

Including extra chemical heating, and thus increasing the gas temperature correspondingly leads to higher CO_2 infrared flux. However, as the increased temperature lowers the CO_2 abundance, the flux ratio between water lines and the main CO_2 feature decreases. As a result, the model with both water UV-shielding as well as chemical heating comes closest to the observed H_2O-to-CO_2 ratios. The CO_2 in this model remains too bright when compared to the surrounding water emission. However, as noted earlier, the CO_2-emitting region extends farther than the H_2O-emitting region. Additional spectra from different physical structures find similar results (See Appendix B).

Figure 3 also shows the H_2O and CO_2 spectra in the case where we assume that the emission of both is contained radially within the water midplane ice line (see Figure 1), perhaps due to the vertical cold finger effect (Meijerink et al. 2009). This cuts both the H_2O and CO_2 flux, but in general, the CO_2 lines are more strongly impacted than the H_2O lines. In the case of the model with shielding, extra chemical heating, and a truncated emitting region, the model H_2O and CO_2 spectra line up nicely with the slab-model spectra that are representative of the Spitzer-IRS observations.

4. Discussion

4.1. CO₂ Column

The thermochemical model with water UV-shielding and chemical heating consistently predicts a CO_2 column in the surface layers that is around 10^{16} cm^{-2}. This is orders of magnitude lower than the 10^{18} cm^{-2} columns that follow from the models that do not include water UV-shielding. However, it is on the high end of the observed data where columns span the 3×10^{14}–3×10^{16} cm^{-2}, with additional nondetection implying even lower CO_2 columns. As such, our models are not capturing the full variation in the observed population. They are, however, representative of a significant part of the full population.

The gas temperatures in our model at the outer edge of the CO_2 emission are colder (<500 K) than the inferred temperatures from the CO_2 Spitzer-IRS observations (~700 K; Salyk et al. 2011). This could imply that the radial temperature profile in the disk is impacting the shape of the $01^10–00^00$ Q branch forcing the slab-model fit to a higher temperature, but lower
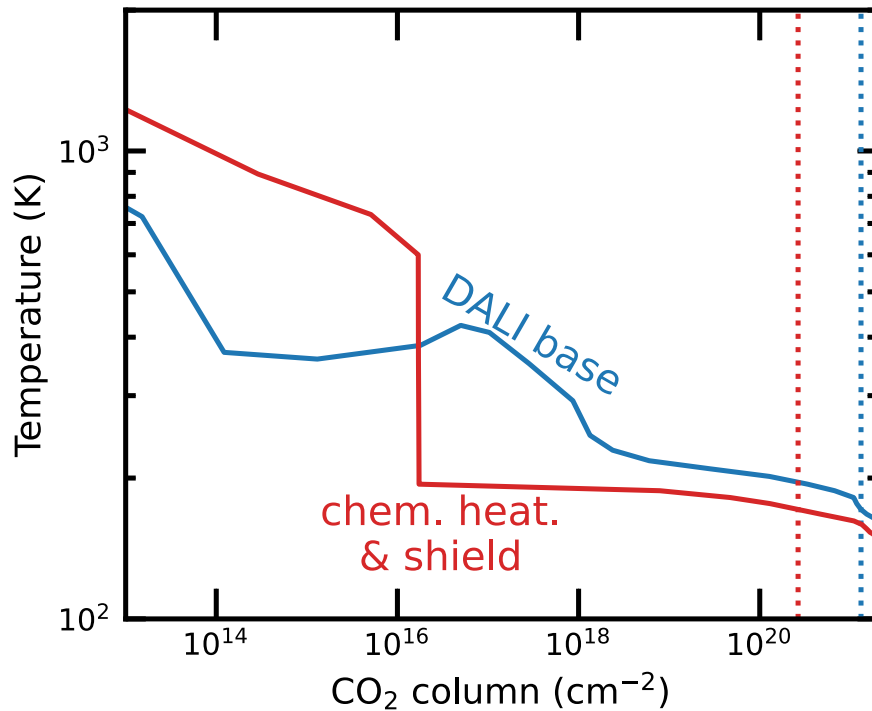
Figure 2. Gas temperature as a function of the cumulative vertical CO_2 column at the location of the midplane H_2O ice line (0.4 au). The CO_2 column is a proxy for the location in the disk, with higher column being deeper into the disk. In the base DALI model, CO_2 is present at a significant abundance over most of the vertical extent of the molecular layer and so the CO_2 temperature changes continuously with increasing CO_2 column or increasing depth. In the heating and shielding model, after reaching a column of about 10^{16} cm^{-2} at a temperature of 600 K, the CO_2 abundance drops significantly. Only very deep into the disk when the temperature has dropped down to 200 K does the CO_2 abundance reach appreciable levels and the vertical CO_2 column increase again with depth. This causes the strong jump in the temperature profile.

column solution. This could also explain why the slab models consistently find a higher gas temperature for the CO_2 than for the H_2O (Salyk et al. 2011), whereas in the models they both emit from the same gas. With individual *P*- and *R*-branch lines of CO_2 and better-isolated lines of H_2O in the JWST-MIRI spectra, it should be possible to get a better handle on the gas temperature and column densities of both these species.

There are chemical pathways that could lead to lower CO_2 abundances. Increasing the gas temperature changes the balance between H_2O and CO_2 formation, which both rely on OH; as a result, a higher temperature lowers the CO_2 abundance. A temperature increase requires either a larger total UV flux or mechanical heating, as currently most of the energy in the UV photons is already converted into heat in the models (Bosman et al. 2022).

Another possible way to lower the CO_2 abundance (and decrease emission) is to increase its destruction rate. Two- and three-body gas-phase reactions that destroy CO_2 are few and inefficient (see Bosman et al. 2018a), whereas reactions due to an ionization source (cosmic rays and X-rays) are already included. This leaves the dissociation of CO_2 due to UV, which already is the main destruction pathway in the surface layers where CO_2 emission is being produced. The current stellar spectrum contains a significant amount of Lyα. The photo-dissociation cross section of CO_2 is modest near Lyα, and CO_2 is not efficiently dissociated in our model (Huestis & Berkowitz 2010; Archer et al. 2013; Heays et al. 2017). However, these cross sections are from measurements at room temperatures. At elevated temperatures, the UV cross section at Lyα increases by up to two orders of magnitude (Venot et al. 2018). Implementing these high-temperature cross sections, however, had little effect on the CO_2 distribution or spectra. In

these models, the CO_2 abundance decreased by 10%–20% in the disk surface layers. As such, we deem that our chemical model is robust in its treatment of CO_2 destruction pathways.

4.2. Tracing the CO_2 Abundance Structure

To properly interpret the CO_2 mid-infrared flux, derive the elemental composition of the gas, and explore disk physical processes, it is important to understand the distribution of CO_2 throughout the disk. The models with water UV-shielding imply that CO_2 will only be present in a thin surface layer and will emit at a similar temperature to water vapor. However, our models predict that water UV-shielding has a strong influence on the CO_2 vertical abundance distribution (Figure 1), which has a significant impact on the column distribution within different thermal layers (Figure 2).

With a higher spectral resolution when compared to Spitzer/IRS, JWST (NIRSPEC and MIRI) offers an opportunity to observe CO_2 vapor with MIRI being able to isolate individual *P*- and *R*-branch lines around 15 μm and potentially detect $^{13}CO_2$ (Bosman et al. 2017). In Figure 4 we predict $^{12}CO_2$ and $^{13}CO_2$ features that can help elucidate the vertical abundance structure of CO_2. In the case without water UV-shielding, there is a significantly higher CO_2 abundance in the deeper layers below the nominal emitting surface region (see, Figure 1). In this case, the relative strength of the two $10^00 - 01^10$ *Q*-branch features at 13.90 and 16.20 μm is high, 20% of the main *Q* branch, while in the model without water UV-shielding, these features are about a factor of 2 weaker. $^{13}CO_2$ emission is also sensitive to these differences; this is in line with previous predictions (Bosman et al. 2017). Conversely, the models predict a nearly constant relative strength of the $01^10 - 00^00$ *P*
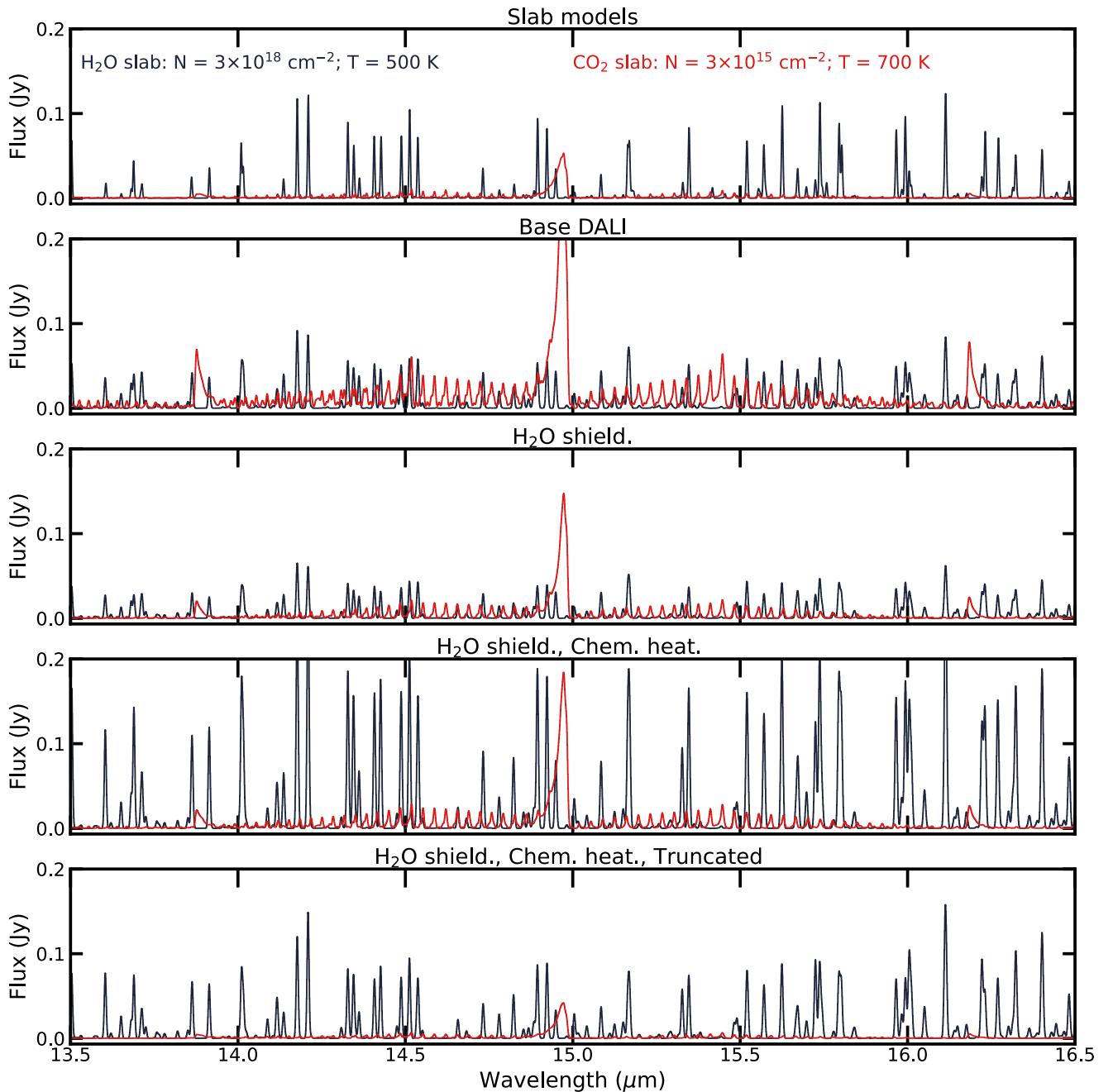
Figure 3. H_2O and CO_2 spectra convolved to an R of 3000 around the CO_2 01^10–00^00 transition. The top panels show slab-model spectra using parameters that reproduce the observational data (Salyk et al. 2011). The four panels below show the DALI output spectra for the thin-disk structure with 99.9% large, settled grains. The second panel shows the base DALI model, the third base DALI with water UV-shielding, the fourth base DALI with water UV-shielding and extra chemical heating, and the fifth panel shows the same model as the fourth panel, now assuming emission can only originate from the region within the water midplane ice line. The slab models clearly predict a CO_2 feature at 15 μm that is weaker than the surrounding water lines, while most DALI models show a brighter CO_2 feature compared to the water lines. Only when combining water UV-shielding, extra chemical heating, and a restricted radial emitting region does the thermochemical flux ratio come close to the observed flux ratio as exemplified by the slab models.

(19)–P(27) and R(19)–R(27) lines, around 10% w.r.t. the main CO_2 Q branch. These lines can thus be used as a yardstick. If the peak of the Q-branch features at 13.90 and 16.20 μm is higher than the 01^10–00^00 rotational lines, this indicates deep, warm CO_2. It should be noted that many of the CO_2 emission features have nearby H_2O lines, which will be blended in observations. Simultaneous fitting of the water spectrum is thus required.

4.3. Radial Extent of the Emitting Layer

In the chemical models, the radial extent of the emitting layer is naturally restricted by the presence of OH. The formation of OH is only efficient at high-enough temperatures that the reaction barrier of the O + H_2 reaction can be overcome. This effectively sets the maximal H_2O emitting area. As chemically CO_2 is linked to H_2O through the presence of OH, CO_2 is thus bound to a similar region from which emission can arise as the H_2O emitting region.
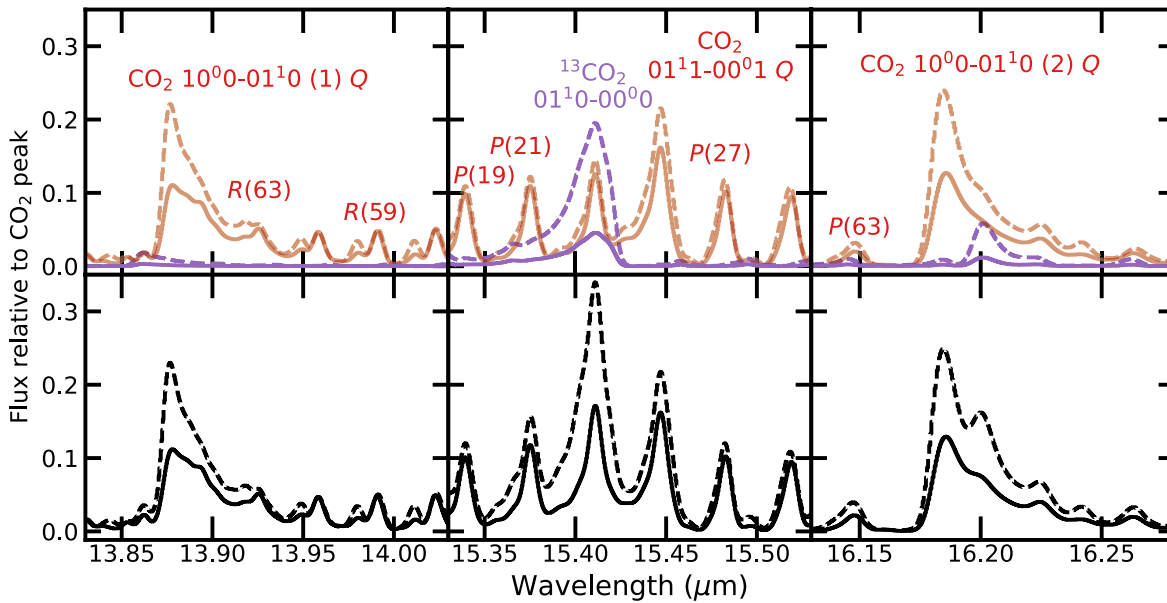
Figure 4. Normalized spectra convolved to $R = 3000$ for the chemical heating model with (solid) and without (dashed) water UV-shielding assuming a thin structure with a surface layer gas-to-dust ratio of 10^5. CO_2 is assumed to only be present within the water midplane radius for all these models. The top panel shows $^{12}CO_2$ and $^{13}CO_2$ in red and purple, respectively. The bottom panel shows the combined spectra. Spectra have been normalizing to the $^{12}CO_2$ 01^10–00^00 Q-branch peak and are zoomed in on three regions with Q branches of interest. While the individual 01^10–00^00 P- and R-branch lines show little differences in normalized flux, the various Q-branch features are impacted by the different abundance structures. Ratios between these can thus be used to derive the deeper abundance structure.
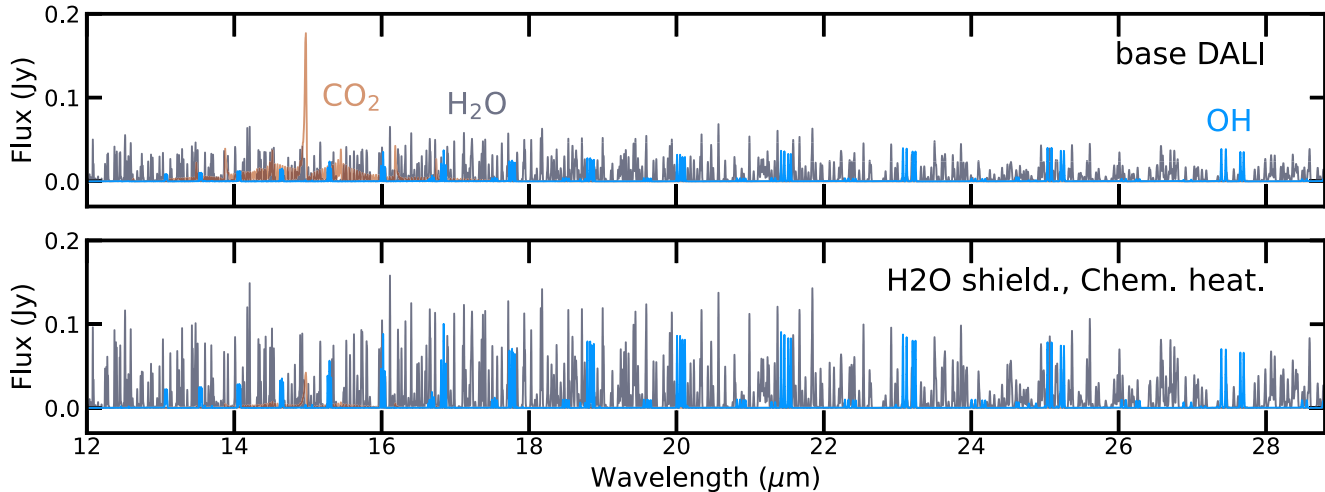
Figure 5. Spectra of OH, CO_2, and H_2O for the base and H_2O UV-shielding and chemical heating models. The emitting region has been constrained to the radial region within the water midplane ice line, and the spectra have been convolved to $R = 3000$. LTE excitation is assumed for OH.

CO_2, however, due to the lower upper-level energies of the main transitions around 15 μm, emits more strongly from colder gas at large radii when compared to water transitions accessible to JWST. This is compounded by the higher CO_2 abundance in colder gas. Radially restricting the emission to warmer gas impacts the CO_2 emission more strongly than the H_2O emission. This can be seen in Figure 3. As the radially restricted emission reproduces the CO_2-to-H_2O flux ratios from the observations. This implies that the emitting areas are actually restricted more tightly than the chemistry implies and that a physical process like the "cold finger effect" is active (e.g., Meijerink et al. 2009; Bosman & Bergin 2021). This process impacts the H_2O directly by mixing it downward and locking up the water in the midplane ices (see, e.g., Krijt et al. 2016). This, in turn, impacts the chemical equilibrium of CO_2 due to the lower availability of oxygen, critical for the

formation of CO_2. As CO_2 is constantly destroyed in the surface layers by UV, any available gaseous CO_2 between the H_2O and CO_2 midplane ice lines will constantly be reprocessed into H_2O, which can then be trapped in the midplane ice. We note that trapping CO_2 in the H_2O ice would still create a CO2-rich atmosphere outside of the H_2O ice line due to the back diffusion of the CO_2 gas (Bosman et al. 2018a).

This could be relatively easily tested by comparing velocity-resolved line profiles of CO_2 and H_2O; unfortunately, CO_2 is hard to do from the ground (e.g., Bosman et al. 2017) and currently there is no planned space mission that will cover this wavelength range with a medium or high spectral resolving power ($\lambda/\Delta\lambda > 10000$). As such, the emitting area from CO_2 will have to be extracted from the analysis of the velocity-unresolved spectra. Comparison with the 4.3 μm band, which can be observed with JWST-NIRSpec, could be helpful here as
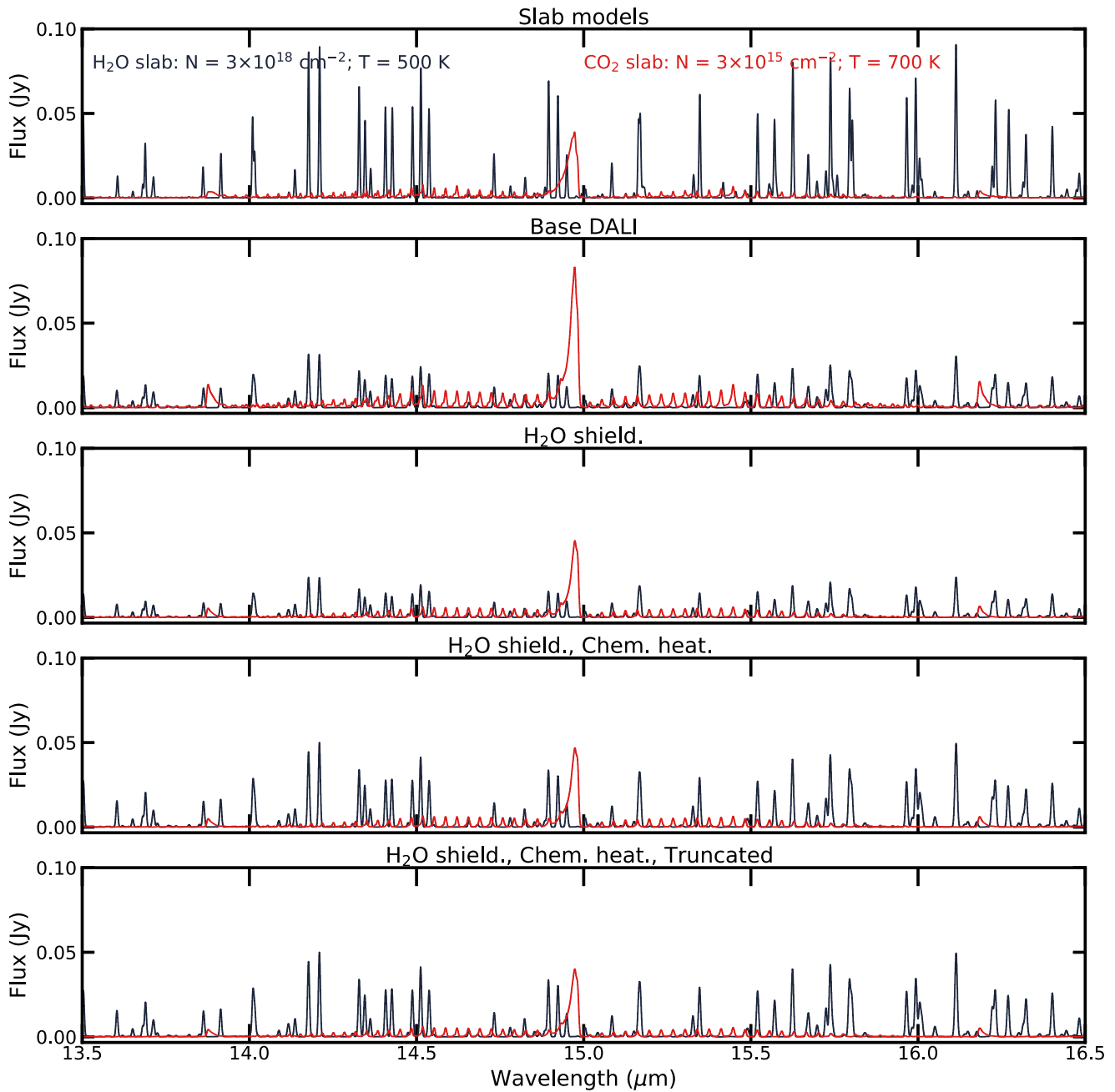
Figure 6. As Figure 3 but from the thin model with a surface layer gas-to-dust ratio of 10^4.

these lines originate from a radially more constrained region and are thus less affected by the abundance of CO_2 outside of the H_2O midplane ice line (see Appendix C). The feature strength ratio between the 4.3 μm band and the 15 μm band could thus be a measure of the radial extent of the total CO_2-emitting region.

5. Conclusions

We study the impact of water UV-shielding and chemical heating on the predicted CO_2 emission arising from within the terrestrial planet-forming zones of gas-rich disks around 15 μm using the thermochemical model DALI. Our base model finds a similar result as found in previously published models (Woitke et al. 2018; Anderson et al. 2021) in that the CO_2 is too bright relative to the H_2O emission.

We find that the water UV-shielding has a strong impact on the CO_2 abundance structure. With UV-shielding included, disk photospheric CO_2 is constrained to a thin layer close to the H/H_2 transition. This yields a CO_2 column of a few times 10^{16} cm^{-2}, two orders less than the CO_2 column prediction without water UV-shielding, $\sim 10^{18}$ cm^{-2}. The lower CO_2 column is in line with the observationally derived column. This suggests that water UV-shielding is present in disk systems, which is consistent with simple conclusions based on the inferred water vapor column (Bethell & Bergin 2009). This large change in column has a strong effect on the CO_2 emission, both in absolute terms, but particularly in the flux ratio between the main isotopologue 01^10–00^00 Q branch on the one hand and the two $10^00 - 01^10$ Q-branch features at 13.90 and 16.20 μm or the main $^{13}CO_2$ Q branch on the other hand.
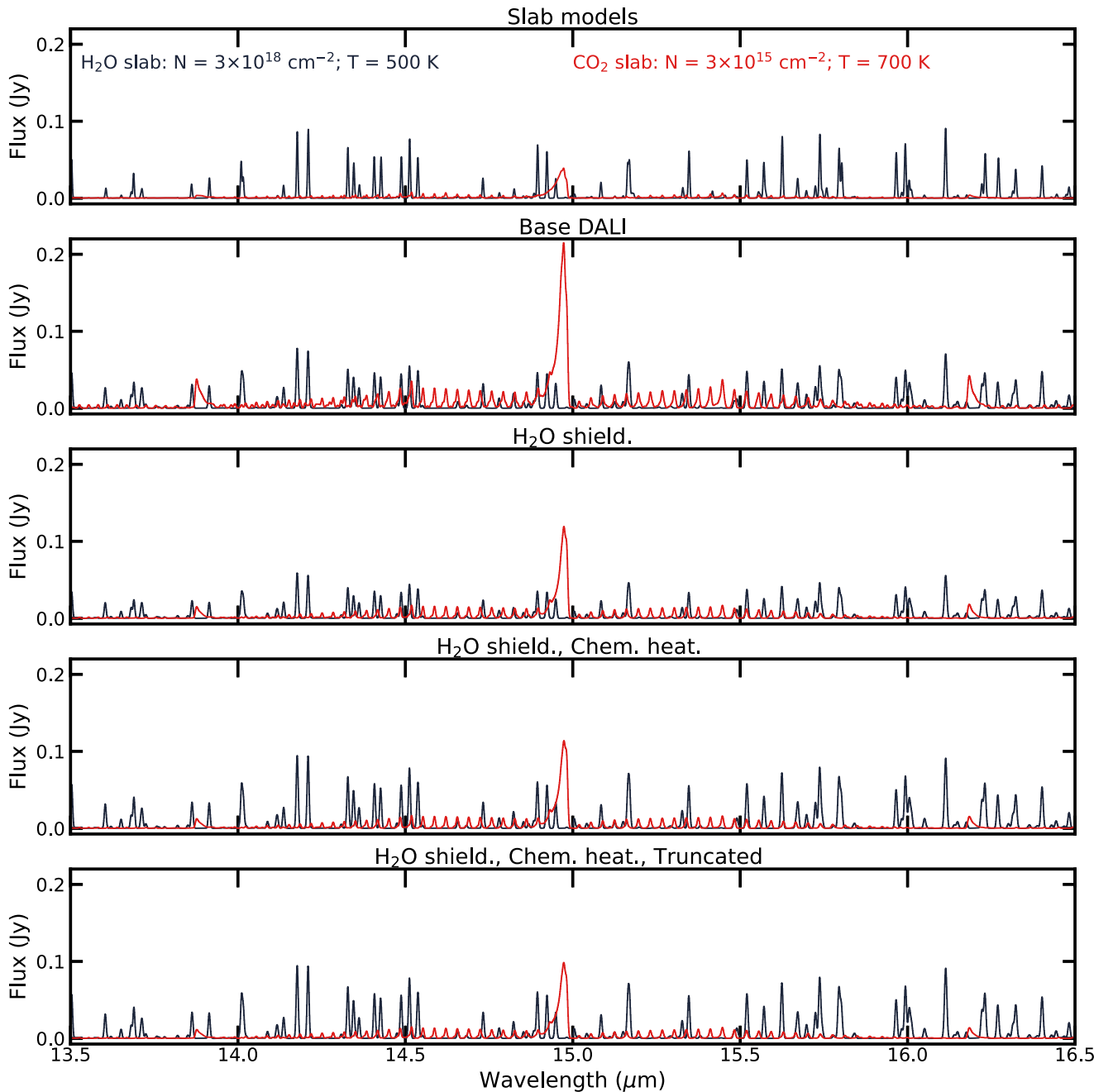
Figure 7. As Figure 3 but from the thick model with a surface layer gas-to-dust ratio of 10^4.

We find the best agreement between thermochemical model spectra prediction and observations if we invoke a radial restriction of the emitting area of both CO_2 and H_2O on top of the inclusion of water UV-shielding and extra chemical heating. The radial restriction increases the average temperature of the emitting gas, which appears to be required by observations. This has an impact on the chemistry, lowering the CO_2-to-H_2O abundance, as well as favoring the H_2O lines relative to the CO_2 lines as the H_2O lines have higher upper-level energies than the main CO_2 lines in the spectra.

We propose that this is evidence of the "cold finger effect", which is the sequestration of oxygen in the form of water in the midplane ice outside of the midplane water ice line. This process would lower the oxygen abundance until the C/O ratio reaches unity, locking all oxygen in CO and preventing the formation of both H_2O and CO_2, which rely on the presence of O or OH, outside of the water midplane ice line, even in the disk atmosphere.
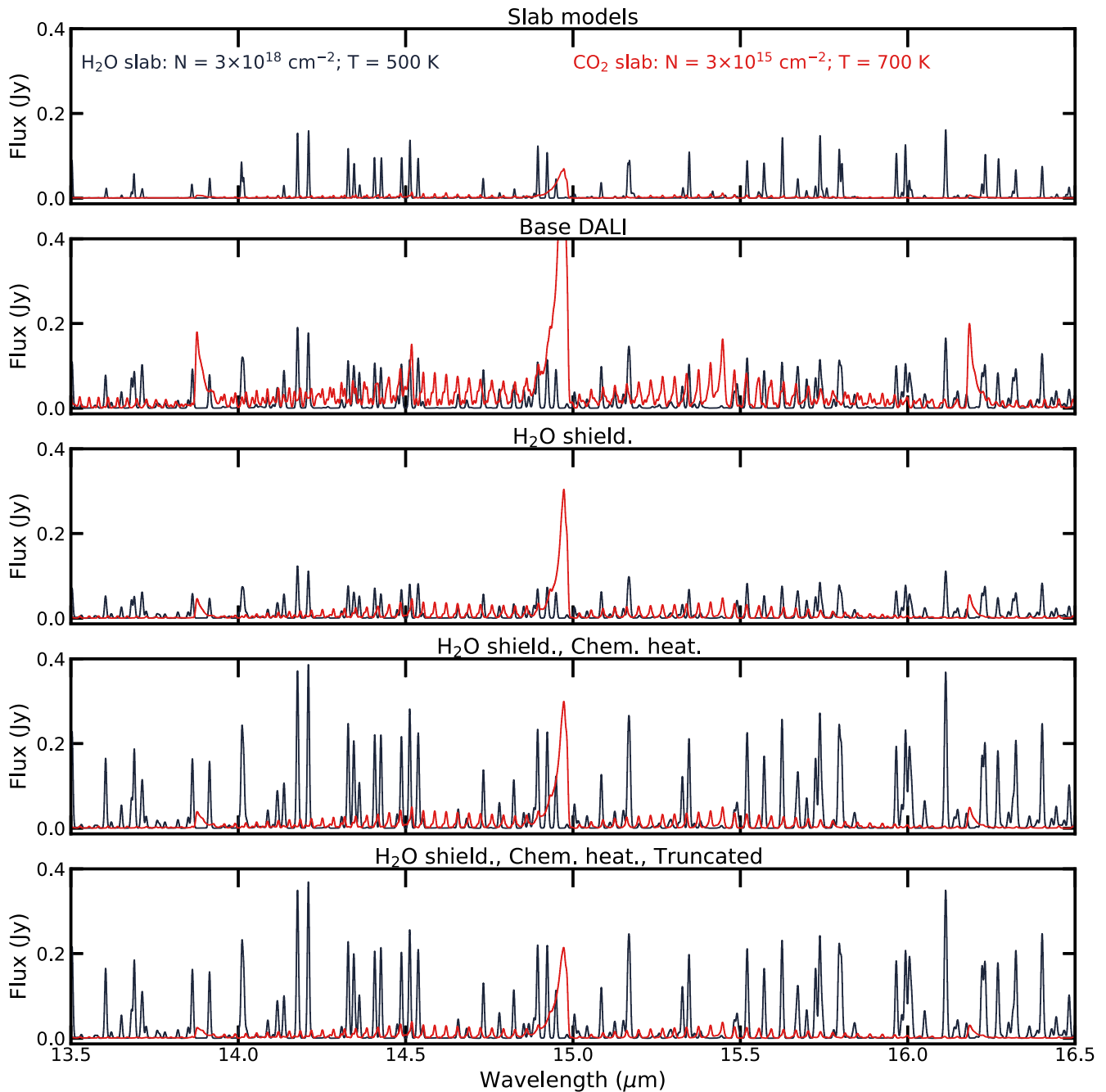
Figure 8. As Figure 3 but from the thick model with surface layer gas-to-dust ratio of 10^5.

Appendix A
OH Spectra

The hydroxide radical, OH, is a critical intermediate in CO, CO_2, and H_2O chemistry. As such, it is worth looking at the effects of H_2O UV-shielding and chemical heating on the OH emission. It should be noted that calculating OH emission is more complex than H_2O and CO_2 emission. H_2O and CO_2 emission are set by collision and radiation equilibrium. OH emission contains a contribution from highly excited OH that is produced in H_2O photodissociation (e.g., Carr & Najita 2014; Tabone et al. 2021). Furthermore OH collisional rate coefficients are not publicly available at present. Therefore, we calculate the OH excitation in LTE. This has an unfortunate side effect that OH emission arises predominantly from low-

density gas at radii >10 au, yielding unrealistically high fluxes with line-to-continuum ratios >10 when convolved to an R of 3000. Fixing all of these issues would be possible with a non-LTE model, and possibly a density-dependent chemical heating rate in the gas, but that is beyond the scope of this paper. As such, we only consider a model with the OH abundance truncated to within the water midplane ice line and do an inter-model comparison only.

The OH LTE spectra are shown in Figure 5 in comparison to the H_2O and CO_2 spectra. Interestingly, the OH to H_2O line flux seems to be similar between the base and H_2O shielding and heating model. This is due to the OH column barely changing between the two models. The OH column is dominated by OH in the top layers of the atmosphere, when
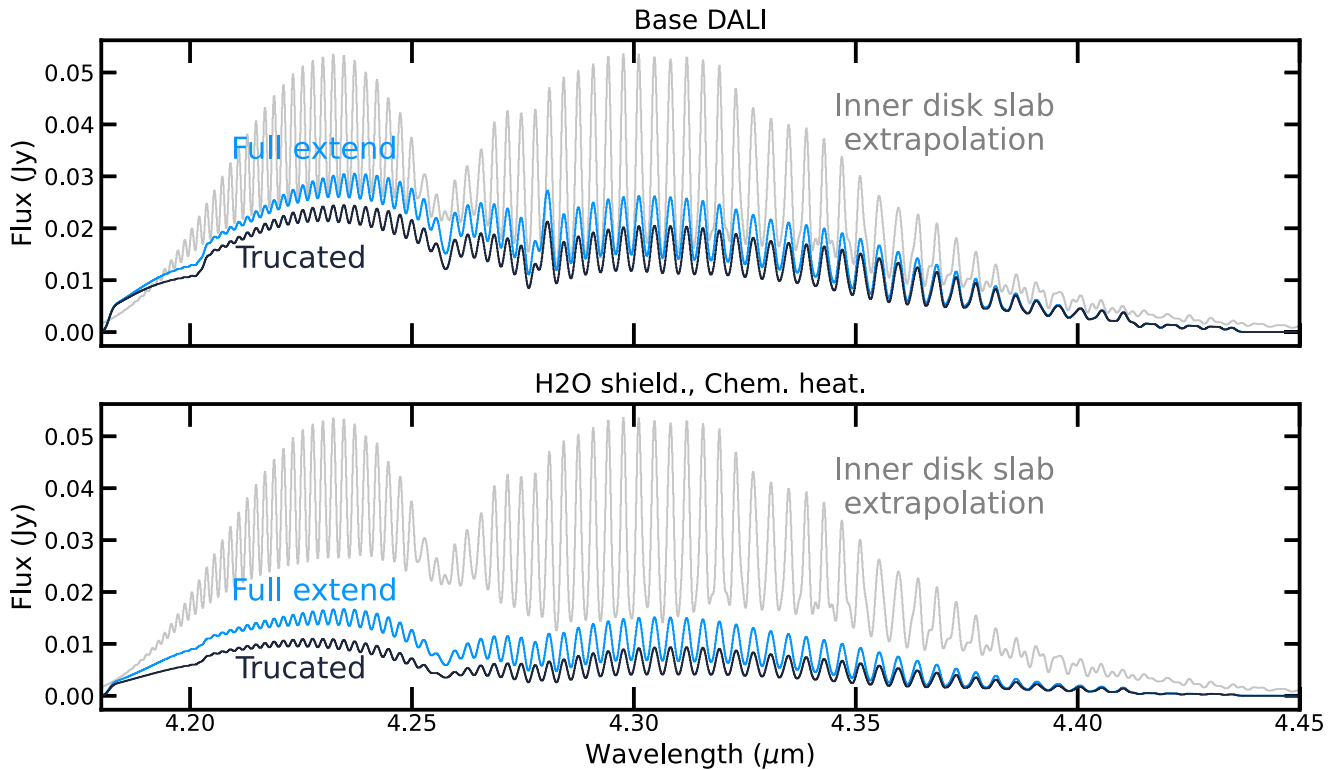
Figure 9. CO_2 spectra around 4.3 μm convolved to $R = 3000$. Most flux is produced by the $00^01(1)$–$00^00(1)$ band, but there also is a contribution of the $01^11(1)$–01^10 (1) band. The top panel shows the spectra including the full extent of the CO_2 emission for base DALI (light blue) and our complete model with H_2O UV-shielding and extra chemical heating. The bottom panel shows the same models, but with the CO_2 emission constrained to within the H_2O midplane ice line. The light gray spectra show the slab model that fits to the observations, using an $N_{CO_2} = 3 \times 10^{15}$ cm^{-2} and $T = 700$K. In contrast to the 15 μm feature, the thermochemical models, are all significantly weaker than the slab model.

the density of H_2 gets high enough to efficiently form H_2O, the OH abundance drops significantly and the OH column barely increases with increasing depth from that point onward. As such, the only difference between the models is the temperature at which OH emits. The temperature change for the OH and H_2O emitting regions are similar, as such their line ratio does not change significantly. However, with the large number of non-LTE effects that can influence the OH emission, it definitely worth looking into OH emission in more detail in a further study.

Appendix B
Model Spectra for Different Physical Structures

Figures 6, 7, and 8 show the H_2O and CO_2 spectra for different variations of the physical structure. The same general trends hold as for the spectra for the reference structure in Figure 3. The variations show, however, that both more dust and a more puffed-up structure lead to a strong CO_2 Q branch relative to the surrounding water lines. More dust leads to lower gas temperatures in the surface layer, which promotes CO_2 production.

Appendix C
Predictions for CO_2 at 4.3 μm

Aside from the strong feature at 15 μm, CO_2 has another strong vibrational band at 4.3 μm corresponding to the asymmetric stretch, the $00^01(1)$–$00^00(1)$ transition. This transition has an upper-level energy of 3350 K and a high Einstein A coefficient (>10 s^{-1}). JWSRT-NIRSpec is likely the

first instrument that will be able to detect this band toward protoplanetary disks. At an $R \approx 3000$, the lines in the bands will not be entirely separated, but the line peaks should be distinguishable (e.g., Bosman et al. 2017). Figure 9 shows the CO_2 model spectra at 4.3 μm.

As with the 15 μm feature, including water UV-shielding and chemical heating lowers the total flux in the CO_2 band, due to the lower CO_2 column in the disk model. Truncating the CO_2-emitting region has less of an effect on the 4.3 μm feature than it has on the 15 μm feature. This is due to the higher upper-level energy of the transition leading to a more centrally weighted emission profile. It is worth noting that in all cases, the predicted 4.3 μm flux from the thermochemical models is below that of the slab model that fits the 15 μm flux. As with the water 6.5 μm emission, this is due to a subthermal excitation of CO_2 in the surface layers of the disk (Bosman et al. 2022). This effect is especially notable as the critical density for the 4.3 μm feature is $\sim 10^{15}$ cm^{-3} (Bosman et al. 2017). As the predicted continuum around 4.3 μm for this model is 0.45 Jy, a high continuum signal-to-noise ratio, >150, is required to detect the full, truncated model.

ORCID iDs

Arthur D. Bosman ⓘ https://orcid.org/0000-0003-4001-3589
Edwin A. Bergin ⓘ https://orcid.org/0000-0003-4179-6394
Jenny K. Calahan ⓘ https://orcid.org/0000-0002-0150-0125
Sara E. Duval ⓘ https://orcid.org/0000-0003-0014-0508

References

Anderson, D. E., Blake, G. A., Cleeves, L. I., et al. 2021, ApJ, 909, 55
Arasa, C., van Hemert, M. C., van Dishoeck, E. F., & Kroes, G. J. 2013, JPCA, 117, 7064
Archer, L. E., Stark, G., Smith, P. L., et al. 2013, JQSRT, 117, 88
Banzatti, A., Meyer, M. R., Bruderer, S., et al. 2012, ApJ, 745, 90
Baulch, D. L., Cobos, C. J., Cox, R. A., et al. 1992, JPCRD, 21, 411
Bethell, T., & Bergin, E. 2009, Sci, 326, 1675
Blevins, S. M., Pontoppidan, K. M., Banzatti, A., et al. 2016, ApJ, 818, 22
Boogert, A. C. A., Gerakines, P. A., & Whittet, D. C. B. 2015, ARA&A, 53, 541
Booth, R. A., Clarke, C. J., Madhusudhan, N., & Ilee, J. D. 2017, MNRAS, 469, 3994
Bosman, A. D., & Bergin, E. A. 2021, ApJL, 918, L10
Bosman, A. D., Bergin, E. A., Calahan, J. K., & Duval, S. 2022, ApJL, 930, L26
Bosman, A. D., Bruderer, S., & van Dishoeck, E. F. 2017, A&A, 601, A36
Bosman, A. D., Tielens, A. G. G. M., & van Dishoeck, E. F. 2018a, A&A, 611, A80
Bosman, A. D., Walsh, C., & van Dishoeck, E. F. 2018b, A&A, 618, A182
Bruderer, S. 2013, A&A, 559, A46
Bruderer, S., van Dishoeck, E. F., Doty, S. D., & Herczeg, G. J. 2012, A&A, 541, A91
Carr, J. S., & Najita, J. R. 2008, Sci, 319, 1504
Carr, J. S., & Najita, J. R. 2014, ApJ, 788, 66
Eistrup, C., Walsh, C., & van Dishoeck, E. F. 2016, A&A, 595, A83
Glassgold, A. E., & Najita, J. R. 2015, ApJ, 810, 125
Heays, A. N., Bosman, A. D., & van Dishoeck, E. F. 2017, A&A, 602, A105

Herczeg, G. J., Wood, B. E., Linsky, J. L., Valenti, J. A., & Johns-Krull, C. M. 2004, ApJ, 607, 369
Huestis, D. L., & Berkowitz, J. 2010, BAAS, 42, 48.13
Hunter, J. D. 2007, CSE, 9, 90
Jonkheid, B., Kamp, I., Augereau, J. C., & van Dishoeck, E. F. 2006, A&A, 453, 163
Krijt, S., Bosman, A. D., Zhang, K., et al. 2020, ApJ, 899, 134
Krijt, S., Ciesla, F. J., & Bergin, E. A. 2016, ApJ, 833, 285
Meijerink, R., Pontoppidan, K. M., Blake, G. A., Poelman, D. R., & Dullemond, C. P. 2009, ApJ, 704, 1471
Mumma, M. J., & Charnley, S. B. 2011, ARA&A, 49, 471
Öberg, K. I., Boogert, A. C. A., Pontoppidan, K. M., et al. 2011, ApJ, 740, 109
Pontoppidan, K. M., Salyk, C., Blake, G. A., et al. 2010, ApJ, 720, 887
Astropy Collaboration, Price-Whelan, A. M., Sipőcz, B. M., et al. 2018, AJ, 156, 123
Astropy Collaboration, Robitaille, T. P., Tollerud, E. J., et al. 2013, A&A, 558, A33
Rothman, L., Gordon, I., Babikov, Y., et al. 2013, JQSRT, 130, 4
Salyk, C., Pontoppidan, K. M., Blake, G. A., Najita, J. R., & Carr, J. S. 2011, ApJ, 731, 130
Smith, I. W. M., Herbst, E., & Chang, Q. 2004, MNRAS, 350, 323
Tabone, B., van Hemert, M. C., van Dishoeck, E. F., & Black, J. H. 2021, A&A, 650, A192
Van Der Walt, S., Colbert, S. C., & Varoquaux, G. 2011, CSE, 13, 22
Venot, O., Bénilan, Y., Fray, N., et al. 2018, A&A, 609, A34
Virtanen, P., Gommers, R., Oliphant, T. E., et al. 2020, Nat. Methods, 17, 261
Woitke, P., Min, M., Thi, W. F., et al. 2018, A&A, 618, A57
Zhang, K., Booth, A. S., Law, C. J., et al. 2021, ApJS, 257, 5